Bert Müller[a], Ricardo Bernhardt[b], Timm Weitkamp[c], Felix Beckmann[d], Rolf Bräuer[e], Uta Schurigt[e], Annelies Schrott-Fischer[f], Rudolf Glueckert[f], Michael Ney[g], Thomas Beleites[g], Claude Jolly[h], Dieter Scharnweber[b]

[a] University of Basel, Biomaterials Science Center, Basel, Switzerland
[b] Dresden University of Technology, Max Bergmann-Center for Biomaterials, Dresden, Germany
[c] Forschungszentrum Karlsruhe, Institute for Synchrotron Radiation/ANKA Light Source, Karlsruhe, Germany
[d] GKSS-Research Center, Institute for Materials Research, Geesthacht, Germany
[e] University Hospital Jena, Institute for Pathology, Jena, Germany
[f] Medical University Innsbruck, ORL University Clinics, Innsbruck, Austria
[g] Dresden University Hospital 'Carl Gustav Carus', Department of Otolaryngology, Dresden, Germany
[h] MED-EL, Innsbruck, Austria

# Morphology of bony tissues and implants uncovered by high-resolution tomographic imaging

*Dedicated to Professor Dr. Hartmut Worch on the occasion of his 65th birthday*

Synchrotron radiation-based micro computed tomography contributes to the increasing demand for uncovering non-destructively the microscopic morphology of bony tissues and their interface regions with implants using isotropic spatial resolution in three-dimensional space. Using the microscopic ring structure of otoliths, the coherence-related interplay between density resolution and spatial resolution is demonstrated. The monochromatised, highly intense synchrotron radiation allows analysis of the morphology of arthritic joints without significant beam-hardening artefacts in a quantitative manner. It further enables intensity-based segmentation of metallic implants within bone and thereby to quantitatively study the bone morphology around different kinds of middle and inner ear implants. This knowledge permits improving medical interventions and optimising the implant's design with respect to surface modification, mechanical properties, and shape.

**Keywords:** Synchrotron radiation tomography; Hard tissue; Implant; Otolith; Cochlea

## 1. Introduction

In the field of biomaterials research, approaches employed in materials science increasingly contribute to solving scientific questions in medicine. The advanced understanding of the biological system's response to biomaterials is essential to make significant progress. The surfaces of biomaterials specifically determine the properties for applications as implant or scaffold in tissue engineering. This fact is especially challenging for the response quantification of complex biological systems, i.e. for in vivo experiments. The complexity of these systems results not only from the interplaying of multiple response and regulation mechanisms but also from the geometrical shapes of the biomaterial itself and its direct neighbourhood. Hence, for detailed analysis of the biological reactions, tools must be developed that permit non-destructive investigation. X-rays are the probes of choice for these tools. C. W. Röntgen verified that X-rays are perfectly suited to visualising bony tissues in great detail. The development of tomographic imaging allows non-destructive uncovering of the microstructure with almost isotropic spatial resolution in three-dimensional (3D) space. Consequently, computed tomography is applied in the daily routine of hospitals with huge success. The spatial resolution has reached values well below 1 mm. Sometimes, however, this resolution is not fine enough and beam-hardening phenomena make the analysis of interfaces with implants impossible. Here, synchrotron radiation sources provide the necessary flux to generate monochromatic X-rays of sufficient intensity to perform computed tomography measurements within reasonable periods of time. In the present paper, this method, termed synchrotron radiation-based micro computed tomography (SRμCT), is applied to hard tissues specifically to characterise the ring-like microstructure of otoliths, the morphology of arthritic joints, and the integration of middle ear and cochlear implants.

Otoliths are calcareous structures formed of aragonite crystals ($CaCO_3$) around the organic protein matrix. Essentially they serve for balance and orientation. In teleost fish there are three pairs of otoliths situated in the fluid-filled auditory chambers of the head. They are first produced during the embryonic stages of development as crystalline primordia. After hatching and throughout the life of the organism they increase in size via a process of sequential deposition forming increments. During the first week of growth increments are micrometre wide, increasing in

width with increasing age and growth rate. Periodicity of increment deposition is dependent on several environmental factors including temperature, light periodicity, behaviour, and stress. Under normal conditions the deposition constitutes a daily cycle governed by diurnal behaviour and circadian rhythm to produce a series of increments, which reflect age in days (increment count) and daily growth (increment width). Age estimation from otoliths is widely performed in marine and freshwater biology.

Under light microscopy each increment is a bipartite structure consisting of a light and a dark zone. The light zone is rich in calcium carbonate, whereas the dark zone is protein rich. Depending on the portion of the otolith being analysed, the dimensions, composition, chemistry, and period of formation can vary widely. Abnormal conditions can affect the periodicity and degree of increment deposition and that otolith growth may not reflect somatic growth directly. Currently-used electron and light microscopy methods involve the time-consuming preparation of thin sections with only limited 3D information. Decalcification used in histological methods for inner ear preparations remove the inorganic matrix and hence alter the structure. Because the growth axes within the structure are generally curved, accurate analyses of the whole growth histories from increment widths exposed on a flat surface are flawed. Furthermore, physiological changes occurring during early development, e. g. metamorphosis, lead to disruption of the deposition process making analysis by light microscopy difficult and subjective. If the SRμCT study could reveal details of the internal structure with a spatial resolution of about 1 μm there is the potential to revolutionise the analysis of growth histories from fish and cephalopods.

Dealing with bony tissues usually relates to the musculoskeletal system. Joints play a major role for locomotion and may be affected by chronic-inflammatory systemic diseases, termed rheumatoid arthritis (RA). The disease refers to progressing destruction of cartilage and bony structures within the involved joint and, finally to bone resorption and/or osteoporosis. Osteoclasts are known to resorb the bone substance through increased production of matrix degrading proteases. Apart from collagenases, it is mainly the cysteine protease cathepsin K that plays a crucial role. At present, the specific neutralisation of cathepsin K is considered as a promising therapeutic approach. Transgenic mice expressing the human tumour necrosis factor (hTNFtg) develop spontaneously a strong destructive polyarthritis, which shows histologically many characteristics of the human RA. Therefore, this model seems to be particularly suitable for investigating the mechanisms of arthritic joint destruction. SRμCT gives access to the detailed macro- and micro-morphology of the bony tissues. Consequently, the method supports the deeper understanding of RA and, subsequently, the choice of an optimised patient treatment.

The mammalian hearing organ contains many bony parts including the ossicular chain consisting of stapes and footplate. The destruction of ossicular chain components necessitates replacement with the appropriate middle ear prosthesis to restore hearing. The anchoring of the prosthesis is particularly difficult if inflammatory processes, e. g. cholesteatoma, have destroyed the supra-structure of the stapes, so that only the base or footplate remains. Prostheses often do not reach the necessary stable connection to the footplate. The subsequent possible dislocations cause concurrent hearing loss. Alternatively, one may fix a titanium middle ear implant on the stapedial footplate by using a bio-mimetic coating with extra-cellular matrix components. The bone contact, quantified by different methods, characterises the degree of fixation and thereby the stability. In particular, as the result of the small implants in animal experiments, the histological preparation often yields just one slice per specimen. Because of the problematic location of the implant, the specimen can even be lost. SRμCT helps to master these difficulties. First, the tomography data provide a valuable means for locating the region of interest. Thus, the histological preparation can be planned accordingly. Second, SRμCT allows non-destructive visualisation of the structures down to a few micrometres with almost isotropic spatial resolution [1–5]. Furthermore, SRμCT enables the precise determination of the anatomy. The determinations of the stapes dimensions and morphology can help to optimise the design of the prosthesis and the surgical intervention.

In the mammalian cochlea, sound vibrations (waves) travel along a membrane, peaking at different places where sensory hair cells determine pitch and loudness. The sensory hair cells communicate their responses to the central nervous system via ganglion cells in the cochlea that are able to spike. The possibilities in treating sensorineural hearing loss are restricted. The treatment is often limited to amplification of sound with conventional hearing aids. Cochlear implants offer the possibility to restore some form of hearing in people with profound hearing loss if the cochlear nerve is intact. Cochlear implants mimic lost or non-functional cochlear hair cells by transmitting acoustic stimuli via a microphone/speech processor unit to the inserted electrode. Sound is transformed into a spatial–temporal pattern of electrical impulses that excite spiral ganglion neurons and nerve fibres within the central spindle of the cochlea. The conductive fluids provide the interface with the excitable neural elements [6]. Long electrodes deeply inserted in the scala tympani can stimulate the wide frequency range available in the cochlea. The advantage is due in part by the presence of long nerve fibres in the apical region of the cochlea [7]. The details of the electrical stimulation are complex and include the amplitude, shape, and frequency of the signal used to deliver the charges, the location and design of the electrodes, the tissue impedance and, finally the spiralling geometry of the cochlea. It is difficult for medical doctors to acquire data which allow then to draw conclusions on the integration of the electrode within the cochlea, since it is the hardest human bone. Most histological techniques only provide limited information, since the electrode has to be removed before cutting becomes possible. Therefore, it is necessary to find an alternative method which allows non-destructive visualisation of the implant, the structure of the inner ear, and the temporal bone, simultaneously. The identification of tissue at the implant's interface is the most important but also the most demanding task.

## 2. Experimental

SRμCT in absorption contrast mode is well established for quantitatively characterising the 3D morphology of different kinds of materials and the anatomy of various human

tissues with true micrometre resolution in the three orthogonal directions. The main advantage with respect to conventional μCT is the much higher photon flux, which enables elimination of all photons but the ones of selected energy, and still acquires data in reasonably short time. Bragg reflection by single crystals permits the realisation of a tuneable X-ray source. Because the X-ray absorption coefficient $\mu$ strongly depends on both photon energy $E$ and atomic number $Z$ of the sample, the choice of the photon energy can be optimised minimising the total exposure time at any prescribed sensitivity by the relation $\mu(E, Z) \cdot D = 2$, where $D$ corresponds to the average sample diameter, as shown by Grodzins [8]. The situation becomes much more complex if the specimen is inhomogeneous and consists of different materials. This case is usually the interesting one. Here, higher photon energies than derived from Grodzins' formula provide better results, since star-like artefacts, caused by highly dense components, are reduced.

Coherent micro-radiography measurements of dry otoliths were made at the beamline ID 22 of the European Synchrotron Radiation Facility (ESRF, Grenoble, France). The beamline and the micro-imaging experiment are described in [9]. The photon energy of 14.5 keV was selected with a double-crystal monochromator using the Si(111) reflection. This results in a spectral bandwidth of $\Delta E/E \approx 10^{-4}$. The detector system with a spatial resolution of about 1 μm consists of the scintillator screen that converts the X-rays to an image of a visible wavelength, the microscope optically magnifying the visible-light image, and the charge-coupled device (CCD) camera onto which the magnified image is projected. The scintillator used in this study was a 3.5 μm-thick single-crystal film of europium-doped lutetium aluminium garnet (LAG:Eu), deposited onto an yttrium aluminium garnet (YAG) substrate of 0.17 mm thickness. The CCD camera in this setup is termed FreLoN with $2048 \times 2048$ pixels each 14 μm wide and developed at the ESRF. In combination with the 40-fold magnification of the microscope's optics, this results in an effective pixel size of 0.35 μm and a field of view of $0.7 \times 0.7$ mm$^2$. The detector unit is mounted on a translation stage movable along the optical axis of the X-ray beam, so that the distance between sample and detector can be adjusted.

The tomography experiments were carried out at the beamlines BW 2 and W 2 (HASYLAB at DESY Hamburg, Germany) taking advantage of the standard setup for tomography, which is operated by the GKSS-Research Center Geestacht, Germany [10]. The scheme of the entire experimental setup is given in Fig. 1. Positrons with the energy of 4.5 GeV are forced to travel along a curved path by the bending magnets of the storage ring DORIS III. The wiggler of the beamline BW 2 is a magnetic structure of 28 periods to generate the necessary photon flux. The fixed exit double crystal monochromator, Si(111) provides the monochromatic X-ray beam of desired energy and flux. The sagittally bent second Si(111) crystal reduces the beam divergence and forms a parallel beam about 10 mm wide and 3 mm high. This beam hits the sample at a certain angle and generates the related projection image on the fluorescence screen, which was a 200 μm-thick $CdWO_4$ single crystal. After moderate magnification this optical image is mapped on a Kodak KAF 1600 CCD-chip ($1536 \times 1024$ pixels, pixel length 9 μm) and read out using 14 bit digitalisation at a frequency of 1.25 MHz. The sample manipulator allows precise sample positioning and rotation. For the present study, 721 projections were acquired by rotating the sample in steps of 0.25° from 0 to 180°. In order to eliminate the beam non-uniformities and account for the detector noise, the difference between the individual bare projections and the dark image was divided by the difference of the beam and the dark image to obtain the corrected projections, which were the basis of the reconstruction. Nevertheless, image inhomogeneities still existed due to the photon counting statistics and defects in the fluorescence screen. The reconstruction was performed slice-by-slice with the filtered back projection algorithm [11].

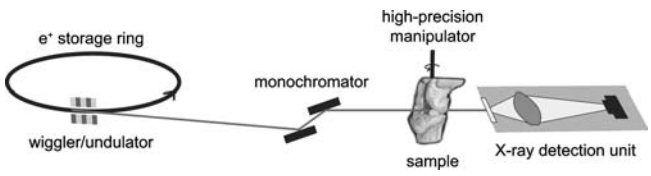


Fig. 1. Charged particles such as positrons that are forced to travel along curved paths with almost light velocity (accelerated motion) emit a white spectrum of highly intense X-rays. Using a double crystal monochromator, almost monochromatic X-rays (spectrum $10^{-4}$) are extracted, which can be applied to image hard human tissues. Reconstructing the sample using the set of images at different angles of incidence, the 3D microstructure of the sample can be uncovered.

The role of the protease cathepsin K in arthritic bone destruction was examined in an animal model of human RA. Therefore, hTNFtg mice were intercrossed with cathepsin K-deficient ($CtsK^{-/-}$) mice to obtain double-mutant animals. In the F2 generation hTNFtg mice, which were cathepsin K-deficient (hTNFtg_$CtsK^{-/-}$), were compared with transgenic mice, which were heterozygous deficient for cathepsin K (hTNFtg_$CtsK^{+/-}$) as well as with non-transgenic animals with homozygous or heterozygous cathepsin K deficiency ($CtsK^{-/-}$ and $CtsK^{+/-}$, respectively). The further genetic background was identical. The bone destruction near the joint (near joint osteoporosis) and the systemic bone destruction (generalised osteoporosis) were examined. For micro-CT analysis knee joints were fixated in paraformaldehyde for about 24 h and embedded without previous decalcification in paraffin.

The embedded samples with a diameter of about 5 mm were measured at the beamline BW 2 using a photon energy of 22 keV. The measurements were carried out using 721 projections and a pixel length of 10 μm. To investigate the differences in the amount of bone along the joint, a procedure was developed to count the bone voxels slice by slice starting from the top of the tibia (details see below). To equalise the anatomical relations of the joints in the tomographic volumes a digital $x-y-z$ rotation was performed. To count only values of mineralised bone, according to the absorption histogram, the absorption levels for bone were transformed into binary data. The first bone contact during a 'down-slice' in the aligned CT-volume was used as the starting point of the analysis. Then, for each slice the binary pixels were summarised and related to the distance from the starting point.

Within another animal study sheep stapes including footplate were extracted from temporal bone and embedded into wax. Samples with a diameter of about 7 mm were measured at the beamline BW 2 using a photon energy of 13 keV. The voxel size is 3.9 μm. The spatial resolution de-

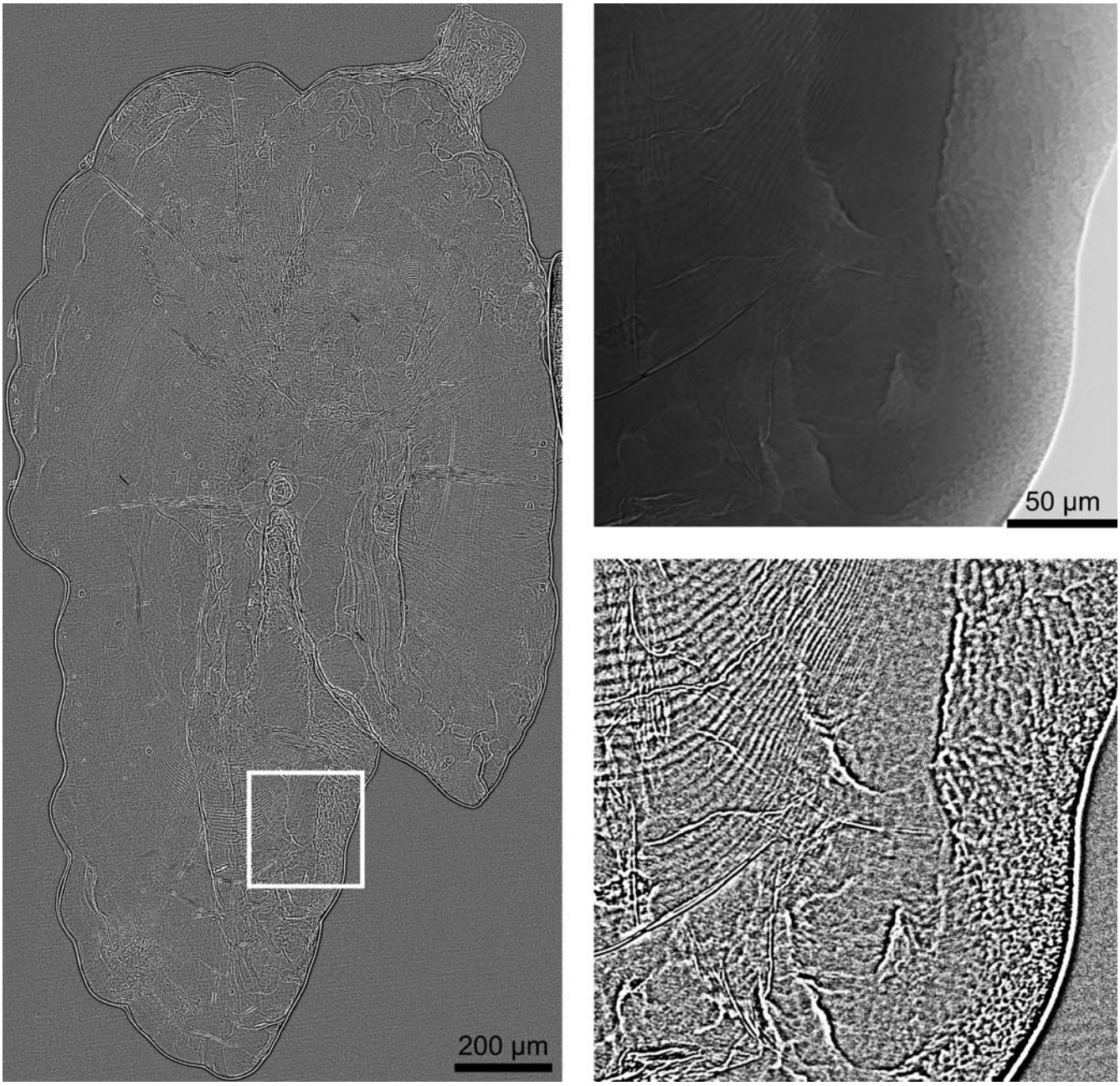


Fig. 2. Phase contrast micro-imaging – projections of the otolith recorded at the ESRF-beamline ID 22 at a photon energy of 14.5 keV. The distance between sample and detector was about 20 mm, so that the edge enhancement becomes clearly visible. The unsharp-mask filtered image on the left is stitched together from 18 raw images. Given the pixel length of 0.35 µm, the image contains much more information than we are able to reproduce here. The detailed images on the right demonstrate the filtering effect.

rived via modulation transfer function of the gold edge [12] corresponds to 12 µm.

The middle ear titanium implants were bio-functionalised by coatings with artificial extra-cellular matrices based on collagen types I and II [13] with immobilised BMP-4 and TGF-β and fixed on sheep middle ear footplates for three months. The extracted footplates together with the implants were wax-embedded.

The SRµCT measurements required a photon energy of 22 keV because of the high absorption of the implants. For each sample 721 projections with a spatial resolution of 12 µm were acquired. The presentation of absorption for bone and titanium is based on the histograms analysed with the image analysis software ImageJ (National Institutes of Health, USA). For the visualisation the software VGStudio-Max 1.2 (Volume Graphics GmbH, Heidelberg, Germany) was applied. The various components in the tomograms were thresholded with intensity-based segmentation. Remaining noise, which derives from the overlap of the absorption levels of tissue and embedding material, was reduced with the structural image filter of ImageJ (noise/despeckle) retaining the overall bone structure.

Another study is included to demonstrate the power of SRµCT in the post-operative characterisation of an inner ear implant. The cochlear implant with surrounding tissue was removed 36 h after the death of the patient and fixated in Karnowsky's formaldehyde–glutaraldehyde solution. The temporal bones needed to be reduced in size for imag-

ing by means of diamond drillers. In order to improve the density resolution of the soft tissues, the entire specimen was post-fixated with 1 % $OsO_4$ for two hours. The temporal bone was placed and fixed in a suitable container. It was entirely filled with the fixation solution and glued to the high-precision rotation stage of the experimental setup. The SRμCT measurements were performed at the beamline W 2. A photon energy of 64 keV was selected. The spatial resolution determined by the modulation transfer function corresponded to 20.7 μm at a pixel size of 8 μm [12]. The experiments were carried out with an asymmetric rotation axis and 360° rotation. For reconstruction by means of the filtered back projection in each case two out of the 1441 projections were combined. To obtain the 3D dataset of the entire implant, 3 tomograms each with $1471 \times 1471 \times 337$ voxels, corresponding to a volume of $23.8 \times 23.8 \times 14.0$ mm$^3$, were combined.

## 3. Results

### 3.1. Otolith micro-radiography

Figure 2 shows the radiograph of the entire otolith stitched together from a set of 18 individual projections. The pixel length of the original radiographs corresponds to 0.35 μm. In order to enhance the visibility of the ring-structures, the projections were spatially filtered by means of the 'unsharp-masking'. This filter makes edges and fine details in the image crisp. It is a simple operator, which subtracts an unsharp (smoothed) version of an image from the original one. The high frequency components in the image, such as the rings of the otolith, become clearer, whereas the low frequency components given by the otolith's outer shape vanish. The two images on the right, which are reproduced with higher magnification, elucidate the effect of this 2D filtering.

The variation of the sample–detector distance modifies the contrast and the spatial resolution in the radiography of the otolith as shown for a selected region of the otolith at the three distances 5, 15, and 35 mm in Fig. 3. The images indicate that the contrast is better for larger distances, but their spatial resolution is superior for smaller distances. Figure 4 shows a quantitative analysis of this trade-off. The presented plot corresponds to the contrast as a function of the spatial frequency for the three selected radiographs. Here, the contrast is computed from the ratio of the power density spectra of the selected radiograph and the related flat field image. Note the power density spectrum of the image is simply the squared modulus of the Fourier transform averaged over all directions in the image.

The maximum values of the three plots given in Fig. 4 indicate that for small distances the contrast increases approximately linearly with the sample – detector distance. The contrast oscillates as the function of the spatial frequency, which is seen best for the plot obtained at the largest sample – detector distance. The spatial resolution decreases with increasing sample – detector distance, as the plots drop at smaller spatial frequencies (see discussion).

### 3.2. Arthritic joints

The SRμCT data clearly show fine morphological details of the arthritic joints (Fig. 5). The inflammation processes led to destruction of the bone in the knee joints. Even the trabe-

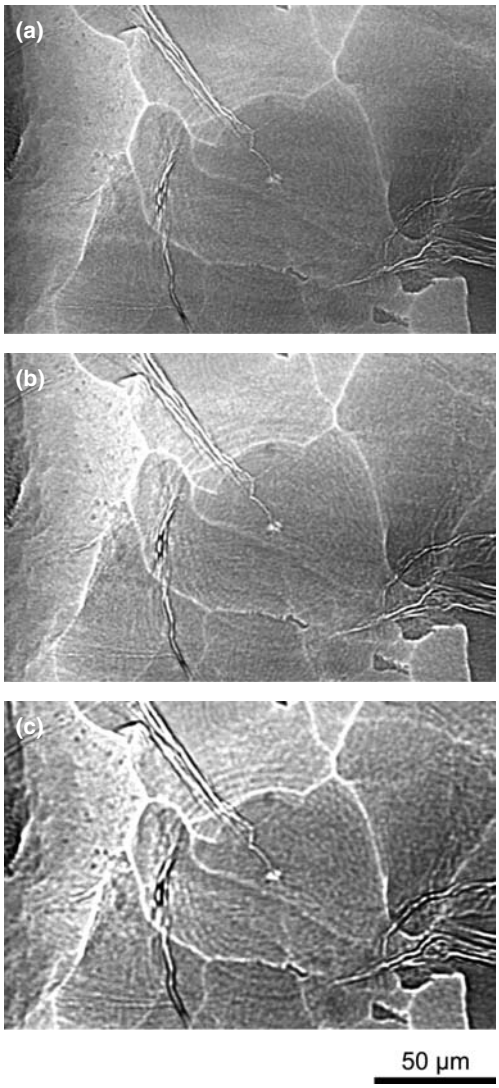


Fig. 3. The three micro-radiographs show a detail of the otolith. The images only differ in the sample-to-detector distance $L_2$ used in the acquisition (A: $L_2 = 5$ mm, B: $L_2 = 15$ mm, C: $L_2 = 35$ mm). It can be clearly seen that with increasing distance the spatial resolution becomes poorer but the contrast increases.

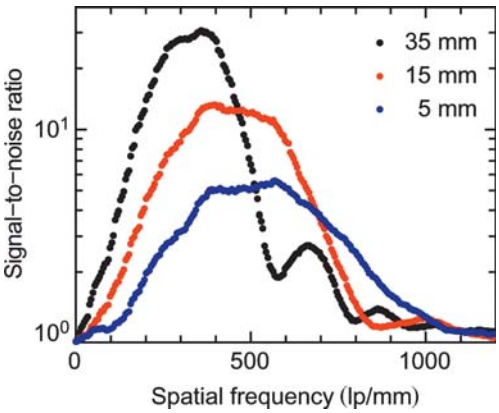


Fig. 4. Signal-to-noise ratio (SNR) for the images shown in Fig. 3 as a function of the modulation frequency $f$, given in line pairs per mm. The SNR was calculated as the ratio of the power density spectrum (PDS) for the corresponding radiograph and the PDS of an image taken under the same conditions, but without a sample in the beam. The curves quantitatively demonstrate the trade-off between spatial resolution and contrast with varying sample-to-detector distance. At higher distances, fine structures, i. e. high frequencies, are less visible, but the SNR for coarser structures increases.

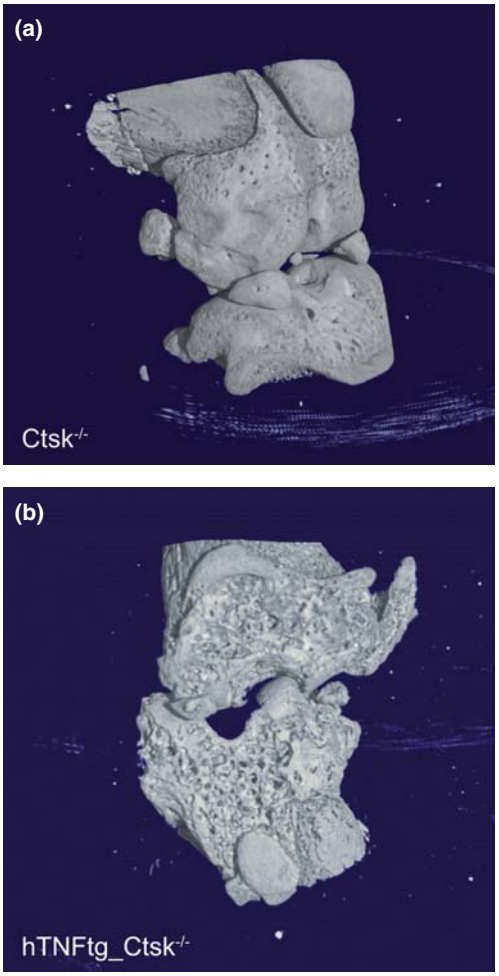


Fig. 5. The 3D representations of arthritic joints exhibit differences and similarities in their morphology, which are characteristic for the treatment of the animals.

cular bone is reduced. The analysis of the morphology allows conclusions to be drawn on the destruction process. The SRμCT investigations show severe destruction of bone and mineralised cartilage in arthritic knee joints of hTNF-transgenic mice with complete cathepsin K deficiency (Fig. 5b) compared to healthy non-transgenic littermates (Fig. 5a).

The tomographic data can be used to analyse the spatial distribution of bone along a selected axis of the joint. One can define a region of interest (ROI), as given in Fig. 6. In each slice, one can integrate the voxels associated with bony tissue. Representing the number of these voxels as the function of slice number or distance to the tibia's top, one finds characteristic curves. Depending on the treatment, the amount of bone is modified. The amount of trabecular bone structures is clearly reduced in transgenic animals independent of the genotype of cathepsin K as demonstrated in Fig. 6b. Non-transgenic cathepsin K-deficient mice ($CtsK^{-/-}$), however, display an osteopetrosis phenotype characterised by an increased number of bone trabeculae in region distant from the top of the tibia (see Fig. 6b).

### 3.3. Middle ear stapes with footplate and titanium implant

SRμCT allows reliable visualisation of the stapes morphology as shown in Fig. 7a. The thickness variations of the

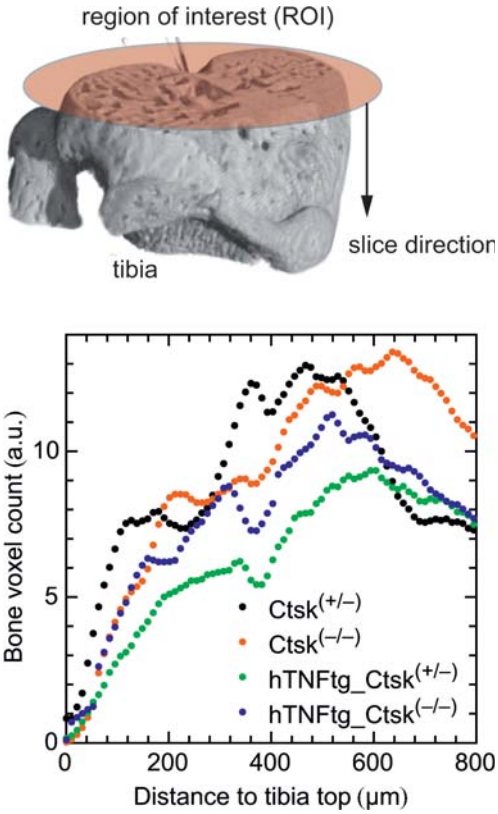


Fig. 6. In the upper part (a) the procedure of the quantitative analysis of the SRμCT data is schematically given. In the lower part (b) the results, i. e. the number of bone-related voxels as the function of distance, are shown quantitatively. The differences between the scatter plots are marginal.

footplate correspond to values between 50 and 200 μm. Figure 7b represents the thickness distribution by means of the colours given in the bar on the right. It should be mentioned that only the absorption values related to mineralised bone are taken into account. The visualisation of the middle ear implant on the footplate, given in Fig. 8, shows an artefact-free representation of the implant geometries. The mineralised tissue and the titanium were segmented to convert the absorption values into binary data. The bio-functionalised implant and mineralised bone can clearly be detected and distinguished.

### 3.4. Cochlear implant

Figure 9 shows the 3D representation of the implant and the bone of the cochlea. The bone is truncated to make visible the implant inside the cochlea. Where the bone is totally removed, the implant, which consists of 12 pairs of oval-shaped electrode contacts and the corresponding platinum wires, is purple coloured. The enveloping silicone matrix of the electrode array is also visible. The implant is intensity-based segmented by means of the software VG Studio Max 1.2 (Volume Graphics, Heidelberg, Germany). It exhibits a complex characteristic shape, since it follows the cochlear spiral that winds up two and a half turns in human. For the inspection of the bone-implant interface, which is of special importance, the bone can be made gradually transparent. This procedure also helps to detect the position of the implant within the inner ear. The fully 3D dataset, that was non-destructively obtained, enables us to perform

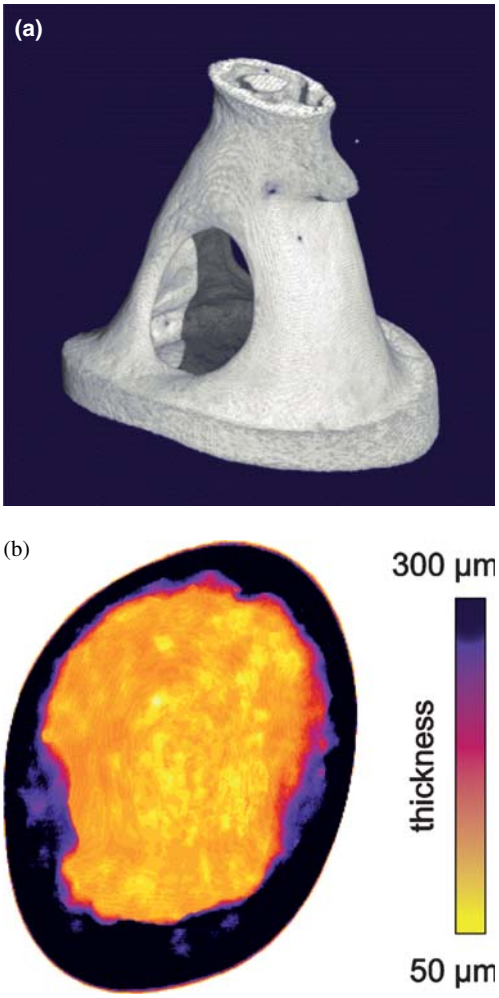


Fig. 7. In the upper part (a) the stapes with footplate using filtered 3D-data from the SRµCT measurement are represented as a 3D image. In the lower part (b) the thickness distribution of the footplate is given using colours according to the bar on the right. The data are based on the integration of absorption values for bone from the top to the bottom of the footplate.

virtual cuts in any desired direction before the histological sectioning is carried out. One can recognise the bony structure of the central modiolus and the electrode (red-coloured), simultaneously.

## 4. Discussion and conclusions

The investigation of otoliths with coherent X-ray microradiography yields their ring-like microstructure by means of inline phase contrast. In order to obtain optimal results, it is crucial to understand the interplay of the three factors determining resolution and contrast in coherent radiography. First, the spatial resolution of the detector, often expressed in terms of the point-spread function in real space or the modulation transfer function in reciprocal space, or, simplified into a single numerical value, in terms of the smallest distance $\delta_{det}$ between two point-like features that can still be resolved as separate according to a properly chosen criterion. The detector resolution value $\delta_{det}$ can obviously not be better than twice the size of a pixel, i.e. 0.7 µm in the present setup. It is also limited by the properties of the visible-light microscope system and of the scintillator. The detector is designed such that these are all

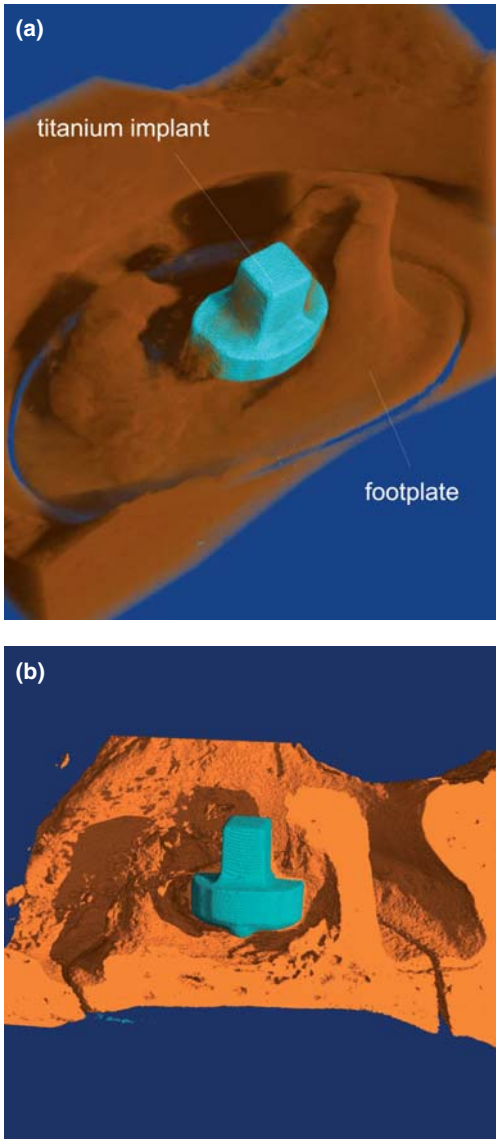


Fig. 8. The upper part (a) shows the 3D-representation of the titanium implant (turquoise coloured) fixed on the stapedial footplate (red-bay-coloured). The implant and its bone contact areas are visible. In the lower part (b), the prominent areas of fully mineralised bone are elucidated by the orange colour visualised from a different angle of view.

matched with respect to each other, resulting in a detector resolution slightly better than 1 µm. Second, penumbral blurring due to the non-zero source size, also known as partial transverse coherence results in an intensity distribution in the detector plane that is blurred by convolution with the source intensity distribution demagnified by the factor of $L_2/L_1$, where $L_1$ is the distance between source and sample, and $L_2$ the distance between sample and detector. ESRF is a third-generation storage ring, characterised by a small transverse size of the electron beam. Combined with the small beam divergence of the X-rays emanating from the undulator source, which allows realising a long beam path, the effect of penumbral blurring is minimal. In other words, there is a high degree of transverse coherence of the beam illuminating the sample. The radiography setup at ID 22 was located at a distance from the source of $L_1 = 65$ m, and $L_2$ ranged between 5 and 35 mm. The transverse source size of the undulator exhibits a full width at half maximum of approximately 700 µm for horizontal and about 50 µm

in vertical direction. The resulting image blurring due to partial coherence was therefore smaller than 0.4 µm even in the horizontal direction and for the largest distance applied. Consequently, this phenomenon plays a minor role in our experiment. The limited detector resolution dominates. The Fresnel diffraction (inline phase contrast) is the third factor that limits the resolution. In the space between sample and detector, the X-ray wave front propagates. By diffraction at the microstructure of the sample interference fringes appear in the detector plane. In the near field, these fringes take the form of edge enhancement at any interface of the sample, often termed inline phase contrast. This allows visualising structures that show negligible X-ray attenuation and are therefore invisible in conventional absorption radiography. The strength of inline phase contrast oscillates with increasing sample–detector distance $L_2$. In the object plane, i.e. at $L_2 = 0$, the phase contrast for the wave front phase modulation of period $p$ is zero. With increasing distance from the sample, the contrast rises to a maximum at $L_2 = p_2/2\lambda$ and reaches zero again at the distance $L_2 = p_2/\lambda$, only to continue oscillating periodically with propagation distance. This phenomenon is known as the Talbot effect. It was used for the characterisation of X-ray coherence properties [14, 15] or for different phase contrast methods [16].

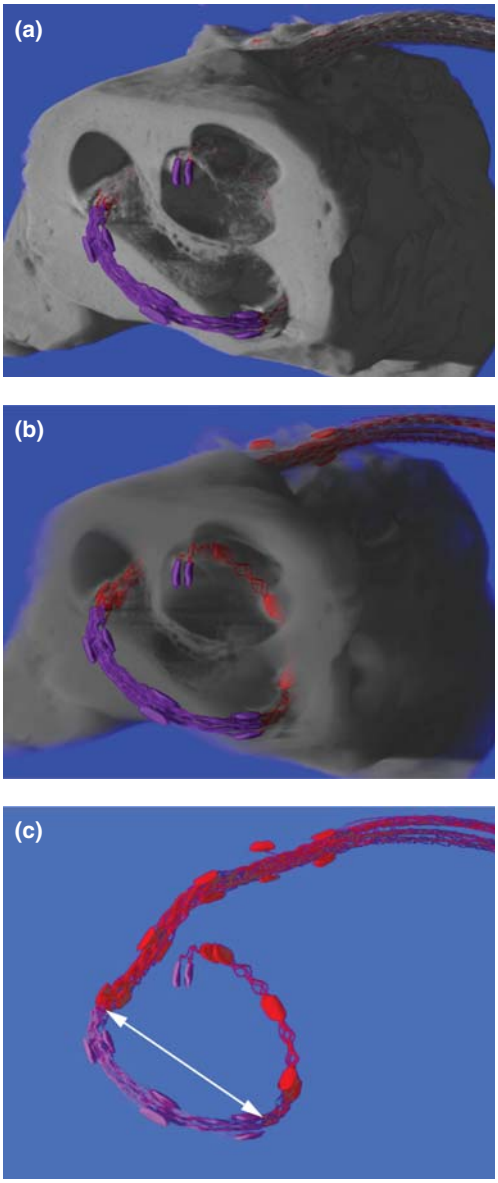


Fig. 9. The metallic part of the cochlear implant is red- and purple-coloured and shows much stronger absorption than the surrounding bone. Therefore, it can be easily segmented. From top to bottom (a to c) the virtually cut bone is made more and more transparent in the selected part. This procedure allows the simultaneous visualisation of the morphology of the bare implant and the surrounding bone. Therefore, the medical doctor can inspect the bone–implant interface and detect potential malfunctions as well as tissue formation in the vicinity of the implant. Note that the indicated length corresponds to 5.1 mm.

The otolith radiographs represented in Fig. 3, which were taken at different sample–detector distances $L_2$, demonstrate the differences in contrast and resolution resulting from the effects discussed above and their trade-off for different distances between sample and detector. The Fourier decomposition of each individual image, namely the power density spectrum shown in Fig. 4, demonstrates the trade-off between contrast and resolution. The smaller the distance $L_2$, the higher the modulation frequency $f = p^{-1}$ that still shows acceptable contrast. But the maximum contrast value for coarser structures increases with $L_2$. The contrast oscillations that are clearly visible in Fig. 4 and best seen for the curve obtained for the largest distance, i.e. $L_2 = 35$ mm, reflect the choice of the experimental parameters: the sample–detector distance and the X-ray wavelength. If one of these parameters is not exactly known, the experimentally determined curves can be used for calibration.

Changes in the bone morphology inside the joints may be an indication of arthritic disease. Histological investigations have already verified arthritic destructions by the use of 2D imaging. With the SRµCT measurement a 3D visualisation of the joint's bone morphology was possible with a spatial resolution on the micrometre scale. The change in the bone volume along a pre-selected path could be quantified with a 3D analysis, starting the procedure at well-defined anatomical landmarks of the joints. Relative changes of the bone volume along this path revealed small differences of the local bone structures for the joints investigated and are in reasonable agreement with the morphological findings. We were unable to find any model for a standardised quantification of the arthritic destruction level in literature. The spatial information of the SRµCT data enables us to select anatomical landmarks and to define procedures for the validity checks of different arthritic models.

The 3D investigation of stapes and footplate from the ossicular chain with SRµCT allows visualisation of the bone morphology in detail. Integrating the spatial absorptions values, a thickness profile for the mineralised bone of the footplate could be generated, which is shown in Fig. 7b. This information is essential for the implant design for two reasons. First, it allows for the selection of an implant geometry with a guaranteed implant–footplate-contact, which is a prerequisite for osteointegration. Second, based on the profile it is possible to realise these contact areas in those regions of the footplate that are expected to show a high potential for osteointegration.

The abilities of SRµCT to visualise the contact area between small titanium implants and the stapedial footplate with different bio-functional coatings were investigated in the sheep model. The tomographic visualisations on the mi-

crometre scale in Fig. 8 show a precise image of the spatial distribution of mineralised bone and the position of the titanium implant with respect to the footplate, which potentially will allow evaluation of the osteogenic potential of different coatings. Furthermore, the spatial information from SRμCT data was used to localise the implant during the subsequently performed histological target-preparations.

With SRμCT in absorption contrast mode, we were able to demonstrate that rather large samples of complex 3D structures such as the metallic cochlear implant consisting of 12 electrodes in hard bony tissue can be evaluated with true micrometre resolution. This resolution allows the detailed analysis of the temporal bone structures of the inner ear and the precise location of the electrode array. The use of only histological techniques results in artefacts because of the necessary cut of the electrode array [17]. Consequently, SRμCT is a unique technique for characterising the integration of metallic cochlear implants. In addition, SRμCT enables us to visualise the newly formed bone as well as the soft tissue formation that impairs cochlear function. This technique provides local data on the composition of bone and soft tissue important for highly anisotropic tissues. Hence, it is useful to create meaningful models of the current spread caused by the cochlear implant and thereby helping to improve its design.

Using monochromatic synchrotron radiation one can uncover nanostructures in bony tissue, which have extensions well below 1 μm, as demonstrated for otolith rings in the present study. Analysing the SR-based tomograms of knee joints, quantitative information on the bone micro-morphology can be extracted with high precision. The use of synchrotron radiation even allows studying the bone-implant interface without any significant artefact. This enables us to optimise implants with respect to macro-morphology and surface and to improve advanced surgical procedures.

The authors thank Martin Bailey (FRS Marine Laboratory, Aberdeen, Scotland) for supplying the otolith and related information. The support of Christoph Rau and Philipp Thurner during the measurements at the beamline ID 22 (ERSF, Grenoble, France), the assistance of Julia Herzen during the experiments at the beamline W 2 (HASYLAB at DESY, Hamburg, Germany) and the help of Anne Kluge (Dresden University Hospital 'Carl Gustav Carus', Department of Otolaryngology) are gratefully acknowledged. The studies were financially supported by ESRF Grenoble (SI-625, LS-1980), HASYLAB at DESY Hamburg (grant II-03-065, I-04-077), the German Ministry for Education and Research (BMBF) (grants 03I4034 A to E), the Deutsche Forschungsgemeinschaft – DFG (grants WO 494/15-1 and SCHA 570/9-1), and the Austrian Science Foundation – FWF (grant 15958).

**References**

[1] R. Bernhardt, D. Scharnweber, B. Müller, P. Thurner, H. Schliephake, P. Wyss, F. Beckmann, J. Goebbels, H. Worch: Eur. Cell Mater. 7 (2004) 42.
[2] B. Borah, E.L. Ritman, T.E. Dufresne, S.M. Jorgensen, S. Liu, J. Sacha, R.J. Phipps, R.T. Turner: Bone 37 (2005) 1.
[3] S. Nuzzo, M.H. Lafage-Proust, E. Martin-Badosa, G. Boivin, T. Thomas, C. Alexandre, F. Peyrin: J. Bone Miner. Res. 17 (2002) 1372.
[4] F. Peyrin, M. Salome, S. Nuzzo, P. Cloetens, A.M. Laval-Jeantet, J. Baruchel: Cell Mol. Biol. (Noisy-le-grand) 46 (2000) 1089.
[5] P. Suortti, W. Thomlinson: Phys. Med. Biol. 48 (2003) R1.
[6] C. Arnoldner, W.D. Baumgartner, W. Gstoettner, J. Hamazavi: Acta Otolaryngol. 125 (2005) 228.
[7] J.B. Nadol Jr., D.K. Eddington: Adv. Otorhinolaryngol. 64 (2006) 31.
[8] L. Grodzins: Nucl. Instrum. Meth. 206 (1983) 541.
[9] T. Weitkamp, C. Raven, A. Snigirev, in: U. Bonse (Ed.) Developments in X-ray Tomography II, Proc. SPIE Vol. 3772 (1999) 311.
[10] F. Beckmann, T. Donath, J. Fischer, T. Dose, T. Lippmann, L. Lottermoser, R.V. Martins, A. Schreyer, in: U. Bonse (Ed.) Developments in X-ray tomography, Proc. SPIE Vol. 6318 (2006) 631810.
[11] A.C. Kak, M. Slaney: Principles of Computerized Tomographic Imaging, Society of Industrial and Applied Mathematics, 2001.
[12] B. Müller, P. Thurner, F. Beckmann, T. Weitkamp, C. Rau, R. Bernhardt, E. Karamuk, L. Eckert, J. Brandt, S. Buchloh, E. Wintermantel, D. Scharnweber, H. Worch, in: U. Bonse (Ed.) Developments in X-ray Tomography III, Proc. SPIE Vol. 4503 (2002) 178.
[13] T. Douglas, S. Heinemann: Biomacromolecules 7 (2006) 2388.
[14] P. Cloetens, J.P. Guigay, C. De Martino, J. Baruchel, M. Schlenker: Optics Lett. 22 (1997) 1059.
[15] F. Pfeiffer, O. Bunk, C. Schulze-Briese, A. Diaz, T. Weitkamp, C. David, J.F. van der Veen, I. Vartanyants, I.K. Robinson: Phys. Rev. Lett. 94 (2005) 164801.
[16] T. Weitkamp, A. Diaz, C. David, F. Pfeiffer, M. Stampanoni, P. Cloetens, E. Ziegler: Optics Express 13 (2005) 6296.
[17] O. Adunka, M.H. Unkelbach, M. Mack, M. Hambek: Acta Otolaryngol. 124 (2004) 807.

(Received March 14, 2007; accepted April 21, 2007)

**Bibliography**

DOI 10.3139/146.101507
Int. J. Mat. Res. (formerly Z. Metallkd.)
98 (2007) 7; page 613 – 621

ISSN 1862-5282

**Correspondence address**

Prof. Dr. Bert Müller
Biomaterials Science Center (BMC), University of Basel
c/o University Hospital, CH-4031 Basel, Switzerland
Tel.: +41 61 265 9660
E-mail: bert.mueller@unibas.ch

You will find the article and additional material by entering the document number MK101507 on our website at www.ijmr.de